

1 **Revision 2**

2 Phase transition boundary between fcc and hcp structures in Fe-Si alloy and
3 its implications for terrestrial planetary cores
4
5
6

7 Tetsuya Komabayashi^{1*}, Giacomo Pesce¹, Guillaume Morard², Daniele Antonangeli²,
8 Ryosuke Sinmyo^{3†}, Mohamed Mezouar⁴
9
10

11 ¹School of GeoSciences and Centre for Science at Extreme Conditions, University of
12 Edinburgh EH9 3FE, UK
13

14 ²Sorbonne Université, Muséum National d'Histoire Naturelle, UMR CNRS 7590, IRD,
15 Institut de Minéralogie, de Physique des Matériaux et de Cosmochimie, IMPMC, 75005
16 Paris, France
17

18 ³Bayerisches Geoinstitut, Universitat Bayreuth, 95440 Bayreuth, Germany
19

20 ⁴European Synchrotron Radiation Facility, BP 220, F-38043 Grenoble Cedex, France
21
22
23

24 *corresponding author: Tetsuya Komabayashi
25 E-mail: tetsuya.komabayashi@ed.ac.uk
26

27 [†]Now at Department of Earth and Planetary Science, University of Tokyo, 7-3-1 Hongo,
28 Bunkyo, Tokyo 113-0033, Japan
29
30

31

ABSTRACT

32 The phase transition between a face-centered cubic (fcc) and hexagonal close-packed
33 (hcp) structures in Fe-4wt% Si alloy was examined in an internally resistive heated
34 diamond anvil cell (DAC) under high-pressure (P) and -temperature (T) conditions to
35 71 GPa and 2000 K by *in-situ* synchrotron X-ray diffraction. Complementary
36 laser-heated DAC experiments were performed in Fe-6.5wt% Si. The fcc-hcp phase
37 transition boundaries in the Fe-Si alloys are located at higher temperatures than that in
38 pure Fe, indicating that the addition of Si expands the hcp stability field. The dP/dT
39 slope of the boundary of the entrant fcc phase in Fe-4wt% Si is similar to that of pure Fe,
40 but the two-phases region is observed over a temperature range increasing with pressure,
41 going from 50 K at 15 GPa to 150 K at 40 GPa. The triple point, where the fcc, hcp, and
42 liquid phases coexist in Fe-4wt% Si, is placed at 90-105 GPa and 3300-3600 K with the
43 melting curve same as in Fe is assumed. This supports the idea that the hcp phase is
44 stable at Earth's inner core conditions. The stable structures of the inner cores of the
45 other terrestrial planets are also discussed based on their P-T conditions relative to the
46 triple point. In view of the reduced P-T conditions of the core of Mercury (well below
47 the triple point), an Fe-Si alloy with a Si content up to 6.5 wt% would likely crystallize
48 an inner core with an fcc structure. Both Venusian and Martian cores are believed to

49 currently be totally molten. Upon secular cooling, Venus is expected to crystallize an
50 inner core with an hcp structure, as the pressures are similar to those of the Earth's core
51 (far beyond the triple point). Martian inner core will take an hcp or fcc structure
52 depending on the actual Si content and temperature.

53

54 **Key words**

55 Earth's core; high-pressure; diamond anvil cell; internal resistive heating; Fe-Si alloy

56

57

INTRODUCTION

58 Terrestrial core formation process has been discussed in relation to
59 metal-silicate equilibration during accretion stage (Li and Agee 1996; Wade and Wood
60 2005; Siebert et al. 2013) although some recent models considered disequilibrium
61 processes at a later stage (Rubie et al. 2011). The metal-silicate equilibration inevitably
62 results in an impure iron rich metallic core (Wade and Wood; Siebert et al. 2013). The
63 impurity includes nickel and several less dense elements which are also called light
64 elements (Poirier 1994; Allègre et al. 1995).

65 Birch (1952) pointed out that the density of pure iron might be greater than the
66 seismological determination for Earth's core. Such a density deficit has been associated

67 with the presence of lighter element(s), and a recent internally consistent
68 thermodynamic model of pure iron estimated the core density deficit to be 7% for the
69 outer core and 4.5 % for the inner core (Komabayashi 2014). Other terrestrial planetary
70 cores also likely contain light elements considering metal-silicate partitioning during
71 their cores formation. In addition, the presence of a magnetic field found in some
72 terrestrial planets may indicate the presence of a light element-bearing partially molten
73 core (e.g., Sohl and Schubert 2007). Light elements would be expelled at the bottom of
74 the liquid outer core as it is less partitioned in the solid inner core and this would drive
75 convection in the outer core (Stevenson et al. 1983; Lister and Buffett 1995).

76 Among the potential light elements, silicon is considered a plausible candidate
77 for the terrestrial planetary cores for various reasons: i) silicon is the second most
78 abundant element in the mantle and series of high-pressure (P) and –temperature (T)
79 experiments demonstrated that silicon and oxygen could be dissolved from mantle
80 silicates to core melt (Takafuji et al. 2005; Ozawa et al. 2009), and then silicon is
81 partitioned between solid and liquid during core crystallization; ii) silicon isotopic
82 composition of stony meteorites is different from bulk silicate Earth (Georg et al. 2007;
83 Fitoussi et al. 2009), implying that silicon might have been partitioned into the core
84 during core-mantle differentiation (Shahar et al. 2011; Hin et al. 2014); iii) all the core

85 formation models based on silicate-metal equilibration inevitably have silicon as a light
86 element in the core (Wade and Wood 2005; Rubie et al. 2011; Siebert et al. 2013).

87 Phase relations and equations of state (EoS) of solid phases in the system
88 Fe-(Fe)Si have been extensively studied by both experiment and theory (Alfe et al.
89 2002; Dobson et al. 2002; Lin et al. 2002; Kuwayama and Hirose 2004; Lin et al. 2009;
90 Tateno et al. 2015; Ozawa et al. 2016). An important phase relation is the transition
91 between face-centered cubic (fcc) and hexagonal close-packed (hcp) structures, as this
92 is central to address the solid inner core structure (Uchida et al. 2001; Asanuma et al.
93 2008; Komabayashi et al. 2009), and the P-T location of the phase boundary can be
94 used to deduce thermodynamic properties (Wood 1993; Komabayashi 2014). Notably,
95 the triple point P-T location where the hcp, fcc, and liquid phases coexist can be
96 constrained from the fcc-hcp boundary and melting curve (Zhang et al. 2016). An
97 experimental study in a laser-heated diamond anvil cell (DAC) reported that the
98 transition temperature was greatly reduced when 3.4 wt%Si was added to Fe (Asanuma
99 et al. 2008). In contrast, phase relations inferred by Fischer et al. (2013) suggested that
100 addition of silicon should increase the transition temperature. Tateno et al. (2015)
101 experimentally demonstrated that the transition temperature was increased by the
102 addition of 6.5 wt%Si to iron. As such the effect of Si on the transition temperature has

103 been a controversy and the P-T conditions of the actual boundaries in the system Fe-Si
104 are not unanimous.

105 In this study, we present the investigation of the P-T locations of the fcc-hcp
106 transition boundaries in Fe-Si alloys in an internally resistive heated DAC. The
107 internally heated DAC heats the sample by its resistance, with an improved accuracy in
108 temperature with respect to conventional laser heated DAC (Komabayashi et al. 2009;
109 2012). Based on these experimental results, we will discuss the effect of Si on the Fe
110 properties under high P-T condition and address the stable structure of a solid Fe-Si
111 alloy at the conditions of the inner cores of the terrestrial planets of the solar system.

112

113 **EXPERIMENTAL PROCEDURE**

114 We conducted high-P-T in-situ X-ray diffraction (XRD) experiments on Fe-Si
115 samples at the beamline ID27, European Synchrotron Radiation Facility (ESRF). X-rays
116 with a wavelength of 0.3738Å were focused to a 3x3 μm^2 spot at sample position and
117 the diffracted X-rays were collected on a two dimensional detector (mar345 Image Plate
118 Detector). The collection time was 10 seconds for each measurement. Using the fit-2D
119 program (Hammersley 1996), the obtained data were converted to the conventional
120 one-dimensional XRD pattern.

121 High pressure was generated in a DAC with a pair of diamond anvils with a
122 culet size of 300 μm or 150-450 μm beveled depending on the pressure range. The
123 starting material was a 5-7 μm thick Fe-Si alloy with 4 wt% Si (Rare Metallic. Co.,
124 hereafter Fe-4Si), placed in the sample chamber and connected to platinum leads. The
125 junction between the Fe sample and Pt leads was outside the sample chamber (see
126 Komabayashi et al. (2009) for the sample geometry). SiO_2 glass layers served as a
127 pressure transmitting medium and thermal insulator. High temperature was achieved
128 with an internal resistive system (Komabayashi et al. 2009; 2012; Antonangeli et al.
129 2012). The sample was resistively heated by directly applying a DC voltage by an
130 external power supply. The temperature was measured by a spectral radiometric system
131 as conventional in laser heating experiments. Noteworthy, thanks to the improved time
132 and spatial stability of the hotspot and the reduced thermal gradients, resulting
133 uncertainties in temperature were about 50 K (Komabayashi et al., 2012)

134 Complementary laser heating experiments were conducted on an Fe-6.5Si
135 sample (Rare Metallic. Co.) at ID27, ESRF (see Morard et al. (2011) for details of the
136 laser heating experimental set up). The internal heating system was not applied because
137 this alloy is so brittle that it was not possible to make it into thin foil. Irrespectively of
138 the use of low numerical aperture and reflecting objectives which effectively minimize

139 the chromatic aberration and improve reliability of temperature determination (Mezouar
140 et al. 2017), the laser heating experiments show larger temperature uncertainty due to
141 large temperature gradient across the sample and laser fluctuations. The two microns
142 diameter pinhole at the entrance of the spectrometer allows for a collection of signal
143 only coming from the very central part of the hotspot and an optimal alignment of lasers
144 and X-ray beam. Morard et al. (2011) discussed that the possible uncertainty in the
145 temperature in this experimental setup might be 150 K at 3000 K. In the present study,
146 we assumed a more conservative number, 10% of the generated temperature.

147 In all the runs, the pressure at any given temperature was calculated with a
148 thermal EoS for Fe-4Si or Fe-6.5Si with the hcp structure that was assessed based on
149 pure iron (Dewaele et al. 2006) and Fe-9wt%Si (Tateno et al. 2015). The room
150 temperature parameters for the Vinet EoS were obtained by averaging on the basis of
151 mole fraction between the two compositions: for Fe-4Si, $V_0 = 22.56 \text{ \AA}^3$, $K_0 = 166 \text{ GPa}$,
152 $K' = 5.4$, and for Fe-6.5Si, $V_0 = 22.63 \text{ \AA}^3$, $K_0 = 167 \text{ GPa}$, $K' = 5.5$, where V_0 , K_0 , K' are
153 the unit-cell volume, bulk modulus, and its pressure derivative at 300 K and 1 bar,
154 respectively. We assumed the same thermal parameters as for pure iron (Dewaele et al.
155 2006; Tateno et al. 2015).

156 The thermal pressure effect on the sample pressure was checked against the

157 pressure for the SiO₂ pressure medium. The EoS for stishovite by Wang et al (2012) was
158 used to calculate the pressure for SiO₂. As the precise temperature for the pressure
159 medium was unknown, we calculated the pressure for SiO₂ at the sample temperature
160 and 300 K. At 42.8 GPa and 1940 K for the sample, the pressure for SiO₂ were 44.9
161 GPa and 34.1 GPa at 1940 K and 300 K respectively. Since the crystallized portion of
162 the pressure medium should be at the same (or slightly lower) temperature of the sample,
163 the above calculation independently supports our pressure determination for the iron
164 alloy. Also, after quench, the pressure for SiO₂ is 37.6 ± 1.0 GPa, which is consistent
165 with the sample pressure of 36.6 ± 0.4 GPa. Therefore, we can conclude that the
166 pressure estimation at high temperatures is reasonable.

167 The use of the unit-cell volume of the hcp phase in the pressure calculation
168 may introduce an uncertainty when the experimental condition is near the completion of
169 the hcp-fcc reaction. Based on a binary temperature-composition (T-X) phase loop
170 detailed below, the pressure could have been underestimated by less than 1.3 GPa at 40
171 GPa and 1870K. When the unit-cell volume for the hcp phase was not obtained, due to
172 either grain growth or complete transition to the fcc phase, we assumed constant
173 pressure upon further heating.

174

175

RESULTS

176 **Fe-4Si**

177 Six separate in-situ XRD experiments were carried out on the Fe-4Si sample in
178 the internally heated DAC. The results are illustrated in Fig. 1a and summarized in
179 Table 1.

180 In the first run, the sample was compressed to 16.4 GPa and the XRD pattern
181 shows coexistence of the bcc and hcp phases. Then the sample was heated to 1060 K
182 and the fcc phase, with a minor amount of hcp phase, was observed. The hcp phase
183 disappeared in the following XRD pattern at a similar temperature of 1050 K.
184 Temperature slightly increased with time to 1080 K at steady power from the DC power
185 supply without further changes in the pattern. Then, we tried to reverse the reaction. As
186 the spectroradiometric method could not reliably measure temperatures below 1000 K,
187 the temperature was estimated based on the linear power-temperature relationship
188 established at 1060 K. During the cooling path, the reversal reaction started at 860 K,
189 200 K lower than the reaction in the forward heating cycle. Further decreasing
190 temperature to 770 K only slightly promoted the reaction, which suggests that
191 nucleation of the hcp phase is very sluggish and implies that the width of the reaction in
192 the backward cycle is much wider than the forward cycle. Accordingly, we constrained

193 the P-T conditions of the reaction in the forward cycle only and the results of the
194 backward cycle are not listed in Table 1 to avoid confusion.

195 In the following runs, we only employed heating cycles which started from the
196 hcp phase towards the fcc stability field. In the runs 2, 3, and 4, we observed a transition
197 sequence from hcp to hcp+fcc and to fcc with increasing temperature. Figure 2 shows a
198 series of XRD patterns collected during the run 2 for increasing temperature at about 24
199 GPa. The temperature was first held at 1120 K for 4 minutes, observing only the hcp
200 phase. Then we increased the temperature to 1230 K and fcc peaks appeared. No further
201 changes in the XRD pattern were recognized during the following 40 minutes, during
202 which the temperature was kept constant. We further increased the temperature to 1260
203 K, which instantaneously increased the intensity of the fcc peaks. During the following
204 30 minutes at constant temperature, the XRD patterns did not show significant changes.
205 The transition was completed at 1330 K. In summary, the drastic changes in XRD were
206 observed only upon temperature increase. The transition from the hcp to fcc phase
207 seems to be very fast, with minimal kinetic effects.

208 In the runs 5 and 6, we observed no structural change to the highest
209 temperatures and confirmed stability of the hcp phase to 71.0 GPa and 2020 K.

210 Overall, thanks to the performances of the internal heating system, we have

211 been able to place tight constraints on the P-T location of the transition boundaries. In
212 particular, the width of the phase loop was accurately constrained. The dP/dT slope of
213 the boundary of the entrant fcc phase in Fe-4wt% Si is similar to that of pure Fe, while
214 the temperature interval of the two-phase region expands with increasing pressure from
215 50 K at 15 GPa to 150 K at 40 GPa (Fig. 1a).

216

217 **Fe-6.5Si**

218 Two separate laser-heating runs were conducted on the Fe-6.5Si sample (Fig.
219 1b). Same as for the internal-heating runs, we increased the temperature under high
220 pressures. In the first run, we compressed the sample to 24.0 GPa at room temperature
221 and then heated it by laser, reporting the appearance of fcc peaks at 1850 K in
222 coexistence with hcp peaks. In the second run, we observed a complete transition to the
223 fcc phase at 2340 K and 56.6 GPa. Considering the uncertainty in temperature in the
224 laser heating experiment (i.e., $\pm 10\%$), the present experimental data are consistent with
225 results by Tateno et al. (2015) (Fig. 1b).

226

227

DISCUSSION

228 **Effect of Si on the fcc-hcp transition**

229 The present experiments confirmed the enlarged high temperature stability of
230 the hcp phase in Fe-4Si and Fe-6.5Si with respect to the case in pure Fe (Fig. 1), in
231 agreement with Fischer et al. (2013) and Tateno et al. (2015) but in contrast to Asanuma
232 et al. (2008). Dissecting the XRD patterns in Asanuma et al. (2008), we noted that they
233 assigned tiny shallow rises as peaks from the fcc phase, while the appearance of the fcc
234 phase is clearly marked by the presence of the (200) peak (Fig. 2) (Komabayashi et al.
235 2009; 2012). We conclude that the transition temperature between the hcp and fcc
236 phases increases with Si content.

237 Figure 3 shows a T-X diagram at 40 GPa based on the present data on Fe-4Si
238 and Fe-6.5Si and existing experimental data on pure Fe and Fe-9Si (Komabayashi et al.
239 2009; Tateno et al. 2015). The fcc-hcp transition temperature increases with Si content.
240 The P-T conditions for a reaction hcp = hcp + B2 phase (Tateno et al. 2015) placed
241 additional constraint on the phase diagram (Fig. 3). The maximum solubility of Si into
242 the fcc phase should be about 7 wt%. A thermodynamic model will be made to fit the
243 data in the near future.

244

245

IMPLICATIONS

246 Figure 4 shows a phase diagram of iron alloys reporting the fcc-hcp boundaries

247 in Fe, Fe-4Si, and Fe-6.5Si, together with the P-T ranges for the cores of Mars and
248 Mercury. Addition of Si to Fe expands the stability of the hcp phase as confirmed by the
249 P-T locations of the fcc-hcp transitions observed in this study, which are consistent with
250 Tateno et al. (2015) based on a laser-heated DAC experiments (Fig. 1b). The triple point
251 where the fcc, hcp, and liquid phases coexist in Fe-4wt% Si is placed at 90-105 GPa and
252 3300-3600 K (the melting curve is assumed to be the same as in Fe as Si inclusion at
253 4wt% level should not significantly affect the melting temperature (Morard et al. 2011)),
254 supporting the idea that Earth's inner core at 330-364 GPa is made up with the hcp
255 phase. Tateno et al. (2015) similarly proposed that the inner core would be made of a
256 sole hcp alloy if the Si content is up to 7 wt.%.

257 More complex can be the cases for the other terrestrial planets of the solar
258 system, namely, Venus, Mercury, and Mars. Due to the lack of seismic data,
259 information about their internal structures heavily depends on the average density. As
260 such, the core density deficit cannot be pertinently discussed. Nevertheless geophysical
261 modelling studies argued for the presence of light elements in the cores and kept this
262 into consideration when simulating planetary core, and in particular when discussing
263 their molten/solid state (Stevenson et al. 1983; Williams and Nimmo 2004; Rivoldini et
264 al. 2011; Dumberry and Rivoldini 2015; Knibbe and van Westrenen 2018). In the

265 following, we will limit our discussion to the Fe-Si-S system. Tsujino et al. (2013)
266 summarized existing thermal models for terrestrial core-mantle boundaries in the
267 system Fe-S (Stevenson et al. 1983; Sohl and Spohn 1997; Fei et al. 2000; Williams and
268 Nimmo 2004) and assessed the adiabats across the cores on the basis of the Grüneisen
269 parameter for pure fcc iron (Fig. 4). The known reduction of the crystallizing
270 temperature of iron by addition of silicon (Kubaschewski 1993; Kuwayama and Hirose
271 2004) implies that the thermal profiles in Fig. 4, which are based on the liquidus of the
272 system Fe-S, can be considered as the maximum estimates for the system Fe-Si-S.

273 Venus' similar size to the Earth implies that its internal structure is
274 differentiated into crust, mantle, and core (Sohl and Schubert 2007). However,
275 contrarily to the Earth, Venus does not have a global magnetic field. The pressure at the
276 center of the planet was estimated to be 295 GPa which is slightly lower than of the
277 Earth and crystallization of the liquid core might have not yet started (Stevenson et al.
278 1983). Since the core pressure is far greater than the triple point pressure in the system
279 Fe-4Si (Fig. 4), when upon secular cooling the inner core will start crystallizing,
280 likewise the Earth, it should take an hcp phase.

281 It is suggested that Mercury has a partially molten iron core as it shows a
282 dipole magnetic field from a spacecraft observation (Ness 1979). Further support of the

283 presence of a liquid portion of the core comes from and the amplitude of its librations
284 (Margot et al. 2005). The suggested thermal structure of Mercurian core modeled on the
285 basis of the system Fe-S argues for a temperature much higher than the fcc-hcp
286 transition in Fe-6.5Si (Fig. 4). Recently proposed thermal models of Fe-Si cores showed
287 a similar temperature range as in Fig. 4 (Knibbe and van Westrenen 2018). Hence
288 Mercurian inner core is expected to take an fcc structure if the Si content is less than 6.5
289 wt%. Only upon further cooling, the fcc-structured alloy in Mercurian inner core, will
290 be transformed to the hcp phase.

291 Mars currently does not have an active global magnetic field, although it has a
292 metallic core in view of its average density and moment of inertia (Yoder et al. 2003).
293 However, the presence of magnetized rock records found in southern highland area
294 indicates that the planet should have had a magnetic field in the past. Stevenson et al.
295 (1983) suggested that present Martian core should still be totally molten to account for
296 the absence of the magnetic field and the rocks were magnetized by a field produced by
297 a past, now extinct, thermal convection of the liquid core. The inferred thermal profiles
298 of the core partially overlap with the fcc-hcp transition in Fe-4Si (Fig. 4). As such the
299 first iron alloy crystal that will crystallize in the future will be either fcc or hcp phase
300 depending on the actual Si content and exact temperature. In the case of the fcc phase, it

301 will be transformed to the hcp phase as the core further cools down.

302 In summary, the inner core structure of the terrestrial planets can be discussed
303 based on the phase relations in Fig. 4. The hcp core would show more anisotropic
304 seismic properties (Steinle-Neumann et al., 2001) than the fcc core because of the
305 anisotropic crystal structure. Also the hcp core would be denser than the fcc core as the
306 fcc-hcp transition in Fe-4Si shows about 0.8% density jump. Those changes are
307 important in future attempts to construct a precise density model for the planetary
308 interior.

309

310

311 **Acknowledgements**

312 The synchrotron experiments were performed at ID27 ESRF. Constructive comments by
313 two anonymous reviewers improved the quality of the manuscript. This research was
314 supported by the European Research Council (ERC) Consolidator Grant to TK (Earth
315 core #647723).

316

317 **References**

- 318 Alfè, D., Gillan, M.J., and Price, G.D. (2002) Composition and temperature of the
319 Earth's core constrained by combining ab initio calculations and seismic data.
320 Earth and Planetary Science Letters 195, 91-98.
- 321 Allègre, C.J., Poirier, J.P., Humler, E., and Hofmann, A.W. (1995) The chemical
322 composition of the Earth. Earth and Planetary Science Letters 134, 515-526.
- 323 Anderson, J.D., Colombo, G., Esposito, P.B., Lau, E.L., and Trager, G.B. (1987) The
324 Mass, Gravity-Field, and Ephemeris of Mercury. Icarus 71, 337-349.
- 325 Antonangeli, D., Komabayashi, T., Occelli, F., Borissenko, E., Walters, A.C., Fiquet, G.,
326 and Fei, Y.W. (2012) Simultaneous sound velocity and density measurements of
327 hcp iron up to 93 GPa and 1100 K: An experimental test of the Birch's law at
328 high temperature. Earth and Planetary Science Letters 331, 210-214.
- 329 Asanuma, H., Ohtani, E., Sakai, T., Terasaki, H., Kamada, S., Hirao, N., Sata, N., and
330 Ohishi, Y. (2008) Phase relations of Fe-Si alloy up to core conditions:
331 Implications for the Earth inner core. Geophysical Research Letters 35, L12307,
332 doi:10.1029/2008GL033863.
- 333 Birch, F. (1952) Elasticity and constitution of the Earth's interior. Journal of
334 Geophysical Research 57, 227-286.

- 335 Dewaele, A., Loubeyre, P., Occelli, F., Mezouar, M., Dorogokupets, P.I., and Torrent, M.
336 (2006) Quasihydrostatic equation of state of iron above 2 Mbar. *Physical Review*
337 *Letters* 97, 215504.
- 338 Dobson, D.P., Vocadlo, L., and Wood, I.G. (2002) A new high-pressure phase of FeSi.
339 *American Mineralogist* 87, 784-787.
- 340 Dumberry, M., Rivoldini, A. (2015) Mercury's inner core size and core-crystallization
341 regime. *Icarus* 248, 254–268.
- 342 Fei, Y.W., Li, J., Bertka, C.M., and Prewitt, C.T. (2000) Structure type and bulk
343 modulus of Fe₃S, a new iron-sulfur compound. *American Mineralogist* 85,
344 1830-1833.
- 345 Fischer, R.A., Campbell, A.J., Reaman, D.M., Miller, N.A., Heinz, D.L., Dera, P., and
346 Prakapenka, V.B. (2013) Phase relations in the Fe-FeSi system at high pressures
347 and temperatures. *Earth and Planetary Science Letters* 373, 54-64.
- 348 Fitoussi, C., Bourdon, B., Kleine, T., Oberli, F., and Reynolds, B.C. (2009) Si isotope
349 systematics of meteorites and terrestrial peridotites: implications for Mg/Si
350 fractionation in the solar nebula and for Si in the Earth's core. *Earth and*
351 *Planetary Science Letters* 287, 77-85.
- 352 Georg, R.B., Halliday, A.N., Schauble, E.A., and Reynolds, B.C. (2007) Silicon in the

- 353 Earth's core. *Nature* 447, 1102-1106, doi:10.1038/nature05927.
- 354 Hammersley, J. (1996) *FIT2D V12.012 Reference Manual*. Eur. Synchrotron Radiat.
355 Facil., Grenoble, France.
- 356 Hin, R.C., Fitoussi, C., Schmidt, M.W., and Bourdon, B. (2014) Experimental
357 determination of the Si isotope fractionation factor between liquid metal and
358 liquid silicate. *Earth and Planetary Science Letters* 387, 55-66.
- 359 Knibbe, J.S., and van Westrenen, W. (2018) The thermal evolution of Mercury's Fe-Si
360 core. *Earth and Planetary Science Letters* 482, 147-159.
- 361 Komabayashi, T. (2014) Thermodynamics of melting relations in the system Fe-FeO at
362 high pressure: Implications for oxygen in the Earth's core. *Journal of*
363 *Geophysical Research* 119, DOI: 10.1002/2014JB010980.
- 364 Komabayashi, T., Fei, Y., Meng, Y., and Prakapenka, V. (2009) In-situ X-ray diffraction
365 measurements of the γ - ϵ transition boundary of iron in an internally-heated
366 diamond anvil cell. *Earth and Planetary Science Letters* 282, 252-257.
- 367 Komabayashi, T., Hirose, K., and Ohishi, Y. (2012) In situ X-ray diffraction
368 measurements of the fcc-hcp phase transition boundary of an Fe-Ni alloy in an
369 internally heated diamond anvil cell. *Physics and Chemistry of Minerals* 39,
370 329-338.

- 371 Kubaschewski, O. (1993) in: Okamoto, H. (Ed.), Phase diagram of binary iron alloys.
372 ASM International, Ohio, p. 380.
- 373 Kuwayama, Y., and Hirose, K. (2004) Phase relations in the system Fe-FeSi at 21 GPa.
374 American Mineralogist 89, 273-276.
- 375 Li, J., and Agee, C.B. (1996) Geochemistry of mantle-core differentiation at high
376 pressure. Nature 381, 686-689.
- 377 Lin, J.F., Heinz, D.L., Campbell, A.J., Devine, J.M., and Shen, G.Y. (2002) Iron-silicon
378 alloy in Earth's core? Science 295, 313-315.
- 379 Lin, J.F., Scott, H.P., Fischer, R.A., Chang, Y.Y., Kantor, I., and Prakapenka, V.B. (2009)
380 Phase relations of Fe-Si alloy in Earth's core. Geophysical Research Letters 36,
381 L06306, doi:10.1029/2008GL036990.
- 382 Lister, J.R., and Buffett, B.A. (1995) The Strength and Efficiency of Thermal and
383 Compositional Convection in the Geodynamo. Physics of the Earth and
384 Planetary Interiors 91, 17-30.
- 385 Margot, J. L., Peale, S. J., Jurgens, R. F., Slade, M. A., and Holin, I. V. (2007) Large
386 Longitude Libration of Mercury Reveals a Molten Core. Science 316, 710-714.
- 387 Mezouar, M., Giampaoli, R., Garbarino, G., Kantor, I., Dewaele, A., Weck, G., Boccato,
388 S., Svitlyk, V., Rosa, A.D., Torchio, R., Mathon, O., Hignette, O., and Bauchau,

- 389 S. (2017) Methodology for in situ synchrotron X-ray studies in the laser-heated
390 diamond anvil cell. *High Pressure Research* 37, 170-180.
- 391 Morard, G., Andrault, D., Guignot, N., Siebert, J., Garbarino, G., and Antonangeli, D.
392 (2011) Melting of Fe-Ni-Si and Fe-Ni-S alloys at megabar pressures:
393 implications for the core-mantle boundary temperature. *Physics and Chemistry
394 of Minerals* 38, 767-776.
- 395 Ness, N.F. (1979) Magnetic-Fields of Mercury, Mars, and Moon. *Annual Review of
396 Earth and Planetary Sciences* 7, 249-288.
- 397 Ozawa, H., Hirose, K., Mitome, M., Bando, Y., Sata, N., and Ohishi, Y. (2009)
398 Experimental study of reaction between perovskite and molten iron to 146 GPa
399 and implications for chemically distinct buoyant layer at the top of the core.
400 *Physics and Chemistry of Minerals* 36, 355-363.
- 401 Ozawa, H., Hirose, K., Yonemitsu, K., and Ohishi, Y. (2016) High-pressure melting
402 experiments on Fe-Si alloys and implications for silicon as a light element in the
403 core. *Earth and Planetary Science Letters* 456, 47-54.
- 404 Rivoldini, A., Van Hoolst, Verhoeven, O., Mocquet, A., Dehant V. (2011) Geodesy
405 constraints on the interior structure and composition of Mars. *Icarus* 213, 451–
406 472.

- 407 Rubie, D.C., Frost, D.J., Mann, U., Asahara, Y., Nimmo, F., Tsuno, K., Kegler, P.,
408 Holzheid, A., and Palme, H. (2011) Heterogeneous accretion, composition and
409 core-mantle differentiation of the Earth. *Earth and Planetary Science Letters* 301,
410 31-42.
- 411 Shahar, A., Hillgren, V.J., Young, E.D., Fei, Y.W., Macris, C.A., and Deng, L.W. (2011)
412 High-temperature Si isotope fractionation between iron metal and silicate.
413 *Geochimica et Cosmochimica Acta* 75, 7688-7697.
- 414 Siebert, J., Badro, J., Antonangeli, D., and Ryerson, F.J. (2013) Terrestrial Accretion
415 Under Oxidizing Conditions. *Science* 339, 1194-1197.
- 416 Sohl, F., and Schubert, G. (2007) Interior structure, composition, and mineralogy of the
417 terrestrial planets, in: Schubert, G. (Ed.), *Treatise on Geophysics*, pp. 27-68.
- 418 Sohl, F., and Spohn, T. (1997) The interior structure of Mars: Implications from SNC
419 meteorites. *Journal of Geophysical Research-Planets* 102, 1613-1635.
- 420 Steinle-Neumann, G., Stixrude, L., Cohen, R.E., and Gülseren, O. (2001) Elasticity of
421 iron at the temperature of the Earth's inner core. *Nature* 413, 57-60.
- 422 Stevenson, D.J., Spohn, T., and Schubert, G. (1983) Magnetism and Thermal Evolution
423 of the Terrestrial Planets. *Icarus* 54, 466-489.
- 424 Takafuji, N., Hirose, K., Mitome, M., and Bando, Y. (2005) Solubilities of O and Si in

- 425 liquid iron in equilibrium with (Mg,Fe)SiO₃ perovskite and the light elements in
426 the core. Geophysical Research Letters 32, L06313,
427 doi:10.1029/2005GL022773.
- 428 Tateno, S., Kuwayama, Y., Hirose, K., and Ohishi, Y. (2015) The structure of Fe-Si alloy
429 in Earth's inner core. Earth and Planetary Science Letters 418, 11-19.
- 430 Tsujino, N., Nishihara, Y., Nakajima, Y., Takahashi, E., Funakoshi, K., and Higo, Y.
431 (2013) Equation of state of gamma-Fe: Reference density for planetary cores.
432 Earth and Planetary Science Letters 375, 244-253.
- 433 Uchida, T., Wang, Y., Rivers, M.L., and Sutton, S.R. (2001) Stability field and thermal
434 equation of state of ϵ -iron determined by synchrotron X-ray diffraction in a
435 multianvil apparatus. Journal of Geophysical Research 106, 21709-21810.
- 436 Wade, J., and Wood, B.J. (2005) Core formation and the oxidation state of the Earth.
437 Earth and Planetary Science Letters 236, 78-95.
- 438 Wang, F.L., Tange, Y., Irifune, T., and Funakoshi, K. (2012) P-V-T equation of state of
439 stishovite up to mid-lower mantle conditions. Journal of Geophysical
440 Research-Solid Earth 117, B06209, doi:10.1029/2011JB009100.
- 441 Williams, J.P., and Nimmo, F. (2004) Thermal evolution of the Martian core:
442 Implications for an early dynamo. Geology 32, 97-100.

- 443 Wood, B.J. (1993) Carbon in the core. Earth and Planetary Science Letters 117,
444 593-607.
- 445 Yoder, C.F., Konopliv, A.S., Yuan, D.N., Standish, E.M., and Folkner, W.M. (2003)
446 Fluid core size of mars from detection of the solar tide. Science 300, 299-303.
- 447 Zhang, D.Z., Jackson, J.M., Zhao, J.Y., Sturhahn, W., Alp, E.E., Hu, M.Y., Toellner, T.S.,
448 Murphy, C.A., and Prakapenka, V.B. (2016) Temperature of Earth's core
449 constrained from melting of Fe and Fe_{0.9}Ni_{0.1} at high pressures. Earth and
450 Planetary Science Letters 447, 72-83.
- 451

452 Figure captions

453

454 Figure 1. Results of the experiments in (a) Fe-4Si and (b) Fe-6.5Si. The phases observed
455 in XRD patterns are plotted: inversed triangle, hcp+bcc; square, hcp; normal triangle,
456 fcc+hcp; circle, fcc. In (a), the boundaries between the fcc and hcp phases in pure iron
457 (Komabayashi et al. 2009) and Fe-3.4Si (Asanuma et al. 2008) are also plotted. The data
458 with asterisk have larger temperature uncertainty. In (b), our data are shown together
459 with experimental data by Tateno et al. (2015). The typical uncertainty (2.5 GPa and
460 200 K) is shown for a guide to the eye, see Table 1 for the uncertainty for each data
461 point. The two datasets are fairly consistent considering the uncertainty in the laser
462 heating experiments.

463

464 Figure 2. Series of XRD patterns collected in the run 2 for increasing temperature. The
465 presence of the fcc phase was unambiguously marked by the appearance of (200) peak.

466

467 Figure 3. Temperature-composition diagram for the fcc-hcp transition. The open circle
468 denotes the transition temperature in pure Fe (Komabayashi et al. 2009); the star
469 symbols are the fcc-hcp reactions constrained by the present experiments; the filled
470 circle is the P-T condition for a reaction of hcp = hcp + B2 phase observed in Tateno et

471 al. (2015). The stability fields of fcc+B2 and hcp+B2 were constrained by phase
472 relations. In particular: (i) the boundary hcp = hcp+B2 should have a negative slope
473 (Tateno et al. 2015) and (ii) the invariant boundary where the fcc, hcp, and B2 phases
474 coexist should be placed at a temperature higher than the upper star at Fe-6.5Si.

475

476 Figure 4. The fcc-hcp boundaries in Fe-4Si and Fe-6.5Si (this study) with phase
477 relations of pure iron (black lines) (Komabayashi et al. 2009; Komabayashi 2014).
478 Thermal profiles of Mercurian and Martian cores in the system Fe-S are also shown
479 (Tsujino et al. 2013).

Table 1. Experimental conditions and results

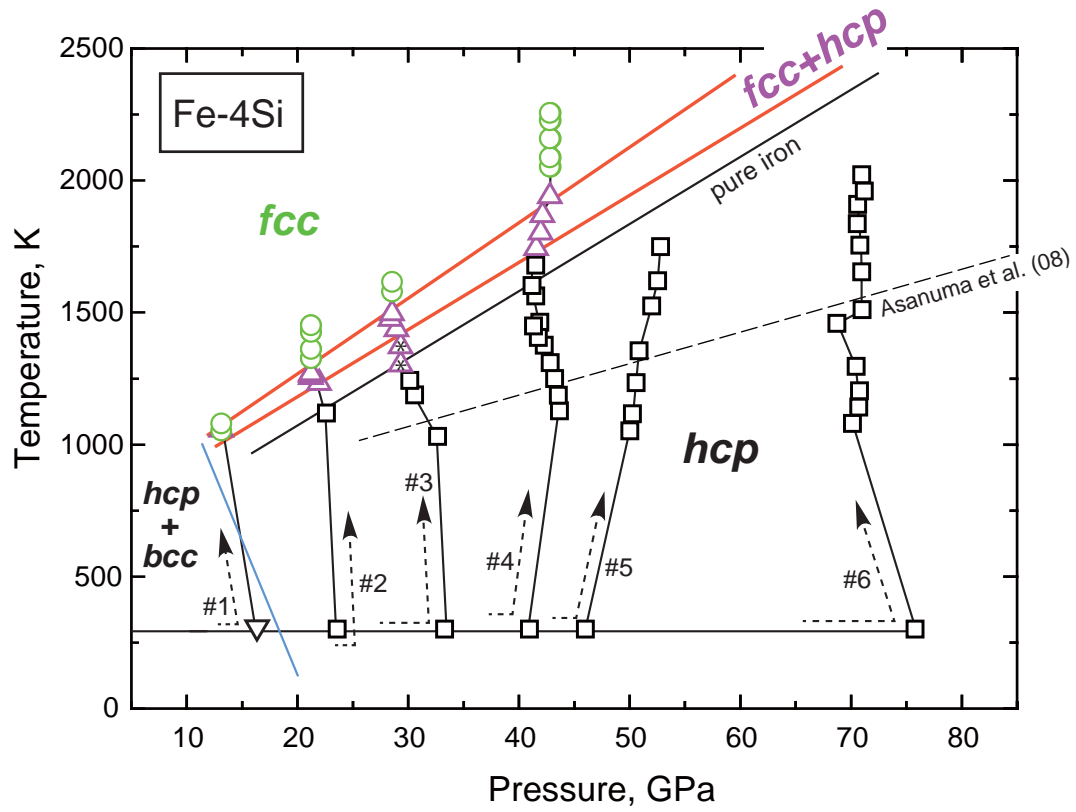
Run	P, GPa	T, K*	Phase	V(hcp), Å ³	a (hcp), Å	c (hcp), Å	V(fcc), Å ³	Remarks
<i>Fe-4Si (internal resistive heating)</i>								
1	16.4(6)	300	bcc+hcp	20.823(53)	2.4640(18)	3.9604(83)		
	13.1(4)	1060	fcc+hcp(small)	21.660(0)	2.4855(0)	4.04853(0)	43.643(14)	
	13.1(4)	1050	fcc				43.615(19)	
	13.1(4)	1080	fcc				43.683(19)	
2	23.6(4)	300	hcp	20.265(27)	2.4394(14)	3.9323(24)		
	22.6(4)	1120	hcp	20.816(3)	2.4554(2)	3.9866(3)		
	21.9(5)	1230	hcp+fcc	20.955(3)	2.4596(2)	3.9998(3)	42.352(0)	
	21.2(4)	1260	hcp+fcc	21.036(0)	2.4596(0)	4.0152(0)	42.343(38)	
	21.2	1260	hcp+fcc	-	-	-	42.330(5)	one peak for hcp
	21.2	1270	hcp+fcc	-	-	-	42.370(4)	one peak for hcp
	21.2	1330	fcc				42.475(15)	
	21.2	1360	fcc				42.520(12)	
	21.2	1430	fcc				42.720(21)	
	21.2	1450	fcc				42.854(69)	
	3	33.3(2)	300	hcp	19.629(11)	2.4193(6)	3.8725(11)	
32.7(5)		1030	hcp	20.016(10)	2.4280(5)	3.9206(10)		
30.6(5)		1190	hcp	20.247(7)	2.4342(4)	3.9456(7)		
30.2(5)		1240	hcp	20.312(9)	2.4361(5)	3.9521(9)		
29.3(1.0)		1300**	hcp+fcc	20.411(13)	2.4399(7)	3.9592(13)	41.463(0)	
29.3(1.1)		1370**	hcp+fcc	20.453(18)	2.4417(9)	3.9611(18)	41.392(0)	
29.0(6)		1440	hcp+fcc	20.524(14)	2.4434(7)	3.9696(14)	41.285(0)	
28.4(1)		1470	hcp+fcc	20.559(5)	2.4465(3)	3.9663(3)	41.344(51)	
28.6(8)		1500	hcp+fcc	20.595(25)	2.4472(14)	3.9710(16)	41.480(37)	
28.6		1580	fcc				41.652(23)	
28.6		1620	fcc				41.650(19)	
4	41.0(5)	300	hcp	19.198(26)	2.3956(14)	3.8626(24)		
	43.7(6)	1130	hcp	19.392(13)	2.4019(7)	3.8813(12)		
	43.6(6)	1190	hcp	19.426(13)	2.4028(7)	3.8852(12)		
	43.3(6)	1250	hcp	19.473(10)	2.4043(5)	3.8899(9)		
	42.8(6)	1310	hcp	19.527(9)	2.4060(5)	3.8949(8)		
	42.3(5)	1380	hcp	19.592(7)	2.4081(4)	3.9011(6)		
	41.9(5)	1460	hcp	19.659(7)	2.4103(4)	3.9074(7)		
	41.8(7)	1410	hcp	19.637(14)	2.4106(8)	3.9021(13)		
	41.4(7)	1450	hcp	19.686(13)	2.4125(7)	3.9056(12)		
	41.5(7)	1560	hcp	19.736(13)	2.4139(7)	3.9111(12)		
	41.2(7)	1600	hcp	19.777(17)	2.4157(9)	3.9133(15)		
	41.5(8)	1680	hcp	19.799(25)	2.4158(13)	3.9173(23)		
	41.6(6)	1740	hcp+fcc	19.833(11)	2.4160(6)	3.9234(10)	39.934(0)	
	42.0(8)	1800	hcp+fcc	19.841(24)	2.4161(13)	3.9247(22)	40.055(0)	
	42.1(9)	1870	hcp+fcc	19.868(28)	2.4175(15)	3.9253(26)	40.080(0)	
	42.8(5)	1940	hcp+fcc	19.868(0)	2.4149(0)	3.9338(0)	40.133(10)	
	42.8	2050	fcc				40.204(13)	
	42.8	2090	fcc				40.216(36)	
	42.8	2160	fcc				40.315(44)	
	42.8	2230	fcc				40.344(43)	
42.8	2260	fcc				40.340(48)		

5	46.0(3)	300	hcp	18.938(15)	2.3856(9)	3.8426(15)	
	50.0(6)	1050	hcp	19.020(12)	2.3882(7)	3.8507(11)	
	50.3(6)	1120	hcp	19.036(10)	2.3885(5)	3.8530(9)	
	50.6(5)	1230	hcp	19.068(7)	2.3890(4)	3.8579(6)	
	50.9(5)	1350	hcp	19.108(4)	2.3897(2)	3.8637(4)	
	52.0(5)	1530	hcp	19.124(5)	2.3901(3)	3.8657(5)	
	52.6(8)	1620	hcp	19.139(17)	2.3904(9)	3.8676(16)	
	52.8(1.3)	1750	hcp	19.186(44)	2.3914(24)	3.8739(41)	
6	75.8(1.2)	300	hcp	17.705(43)	2.3355(25)	3.7481(42)	
	70.1(1.6)	1080	hcp	18.135(48)	2.3563(22)	3.7716(72)	
	70.7(1.5)	1140	hcp	18.133(42)	2.3553(19)	3.7745(62)	
	70.8(1.3)	1200	hcp	18.151(35)	2.3551(16)	3.7789(53)	
	70.5(8)	1300	hcp	18.194(16)	2.3549(7)	3.7886(24)	
	68.7(7)	1460	hcp	18.323(10)	2.3596(5)	3.8000(16)	
	71.0(8)	1510	hcp	18.247(14)	2.3540(6)	3.8025(22)	
	71.0(1.0)	1650	hcp	18.301(21)	2.3552(8)	3.8096(36)	
	70.8(1.0)	1760	hcp	18.347(24)	2.3570(9)	3.8134(42)	
	70.6(1.1)	1840	hcp	18.387(25)	2.3585(9)	3.8169(43)	
	70.6(9)	1910	hcp	18.415(21)	2.3595(8)	3.8193(36)	
	71.2(9)	1960	hcp	18.410(17)	2.3600(8)	3.8169(26)	
	71.0(7)	2020	hcp	18.444(9)	2.3616(4)	3.8187(14)	
	<i>Fe-6.5Si (laser heating)</i>						
1	24.0(1.3)	300	hcp	20.321(14)	2.4382(8)	3.9471(14)	
	28.8(2.3)	1320	hcp	20.539(10)	2.4438(5)	3.9713(9)	
	30.5(2.5)	1520	hcp	20.544(10)	2.4440(5)	3.9717(9)	
	29.6(2.4)	1500	hcp	20.602(9)	2.4457(5)	3.9773(8)	
	28.2(2.3)	1360	hcp	20.612(9)	2.4459(5)	3.9784(9)	
	28.0(2.3)	1430	hcp	20.671(9)	2.4473(3)	3.9854(12)	
	29.5(2.8)	1610	hcp	20.683(36)	2.4465(15)	3.9900(51)	
	29.5(3.1)	1640	hcp	20.695(60)	2.4507(25)	3.9788(82)	
	29.5(2.8)	1750	hcp	20.777(29)	2.4513(10)	3.9927(44)	
	29.5	1850	hcp+fcc	-	-	-	42.569(51) one peak for hcp
2	62.1(3.5)	300	hcp	18.308(55)	2.3616(21)	3.7904(93)	
	64.0(3.9)	1480	hcp	18.620(32)	2.3702(10)	3.8271(57)	
	64.0(3.7)	1600	hcp	18.664(20)	2.3702(6)	3.8364(37)	
	63.7(3.6)	1690	hcp	18.717(11)	2.3703(3)	3.8468(19)	
	66.0(5.3)	1930	hcp	18.711(77)	2.3733(8)	3.8360(157)	
	59.5(6.6)	2040	hcp	19.064(158)	2.3848(13)	3.8706(318)	
	53.0(3.5)	2140	hcp	19.456(0)	2.3960(0)	3.9134(0)	
	56.6(3.6)	2240	hcp	19.309(0)	2.3859(0)	3.9169(0)	
	56.6(3.6)	2340	fcc	-	-	-	39.548(156)

* The uncertainty in temperature in the resistive and laser heating are typically 50 K and 10%, respectively.

** Temperature uncertainty is as large as ± 100 K.

a



b

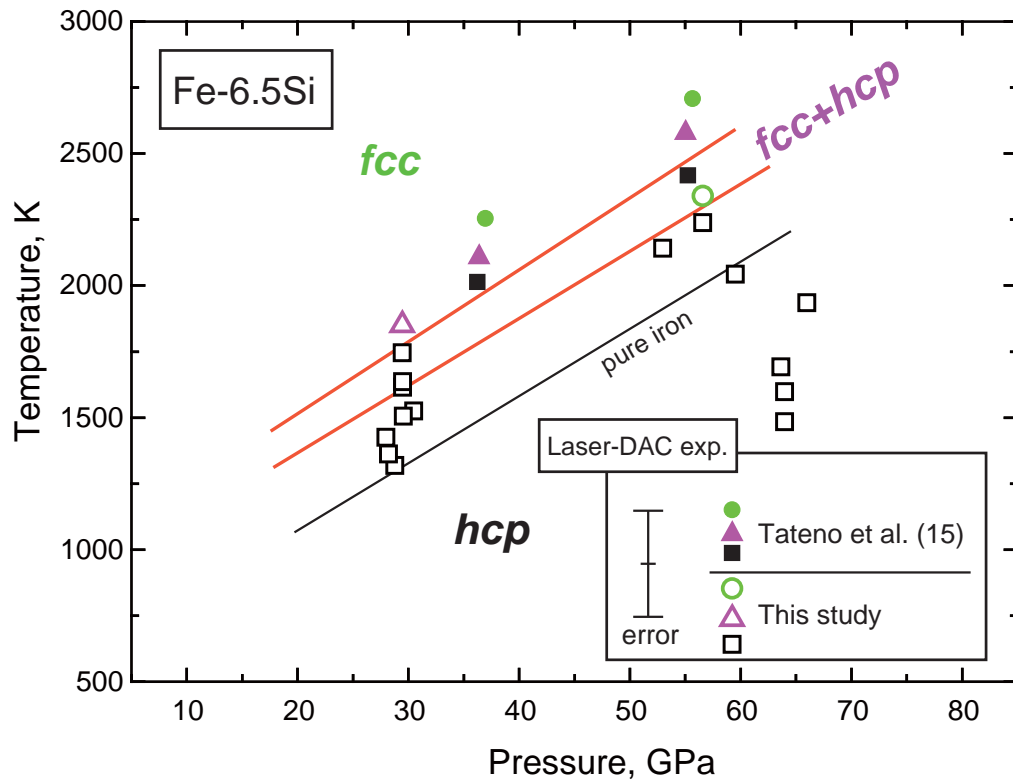


figure 1

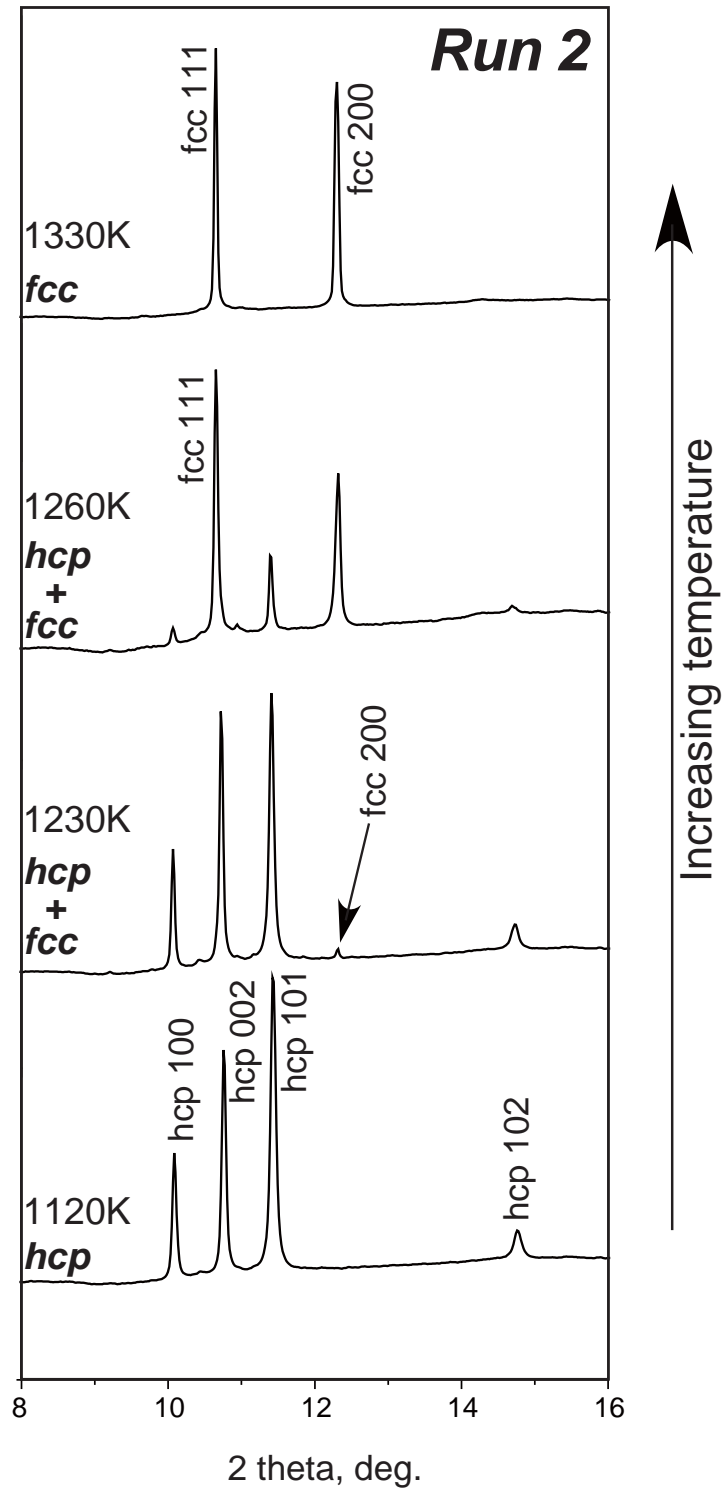


figure 2

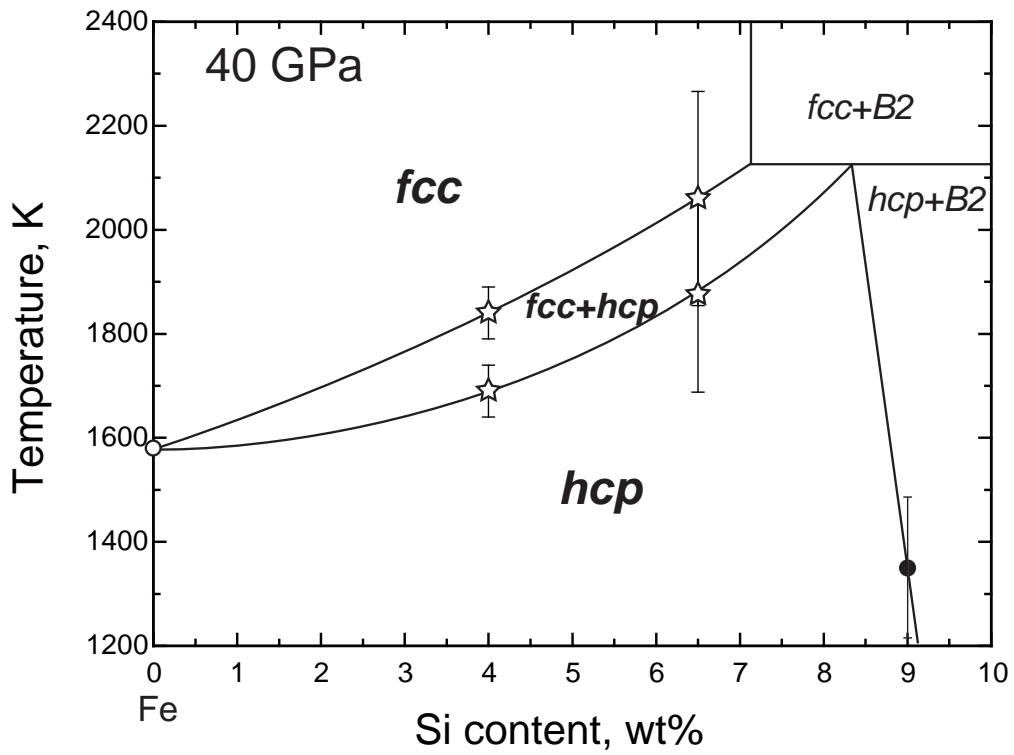


figure 3

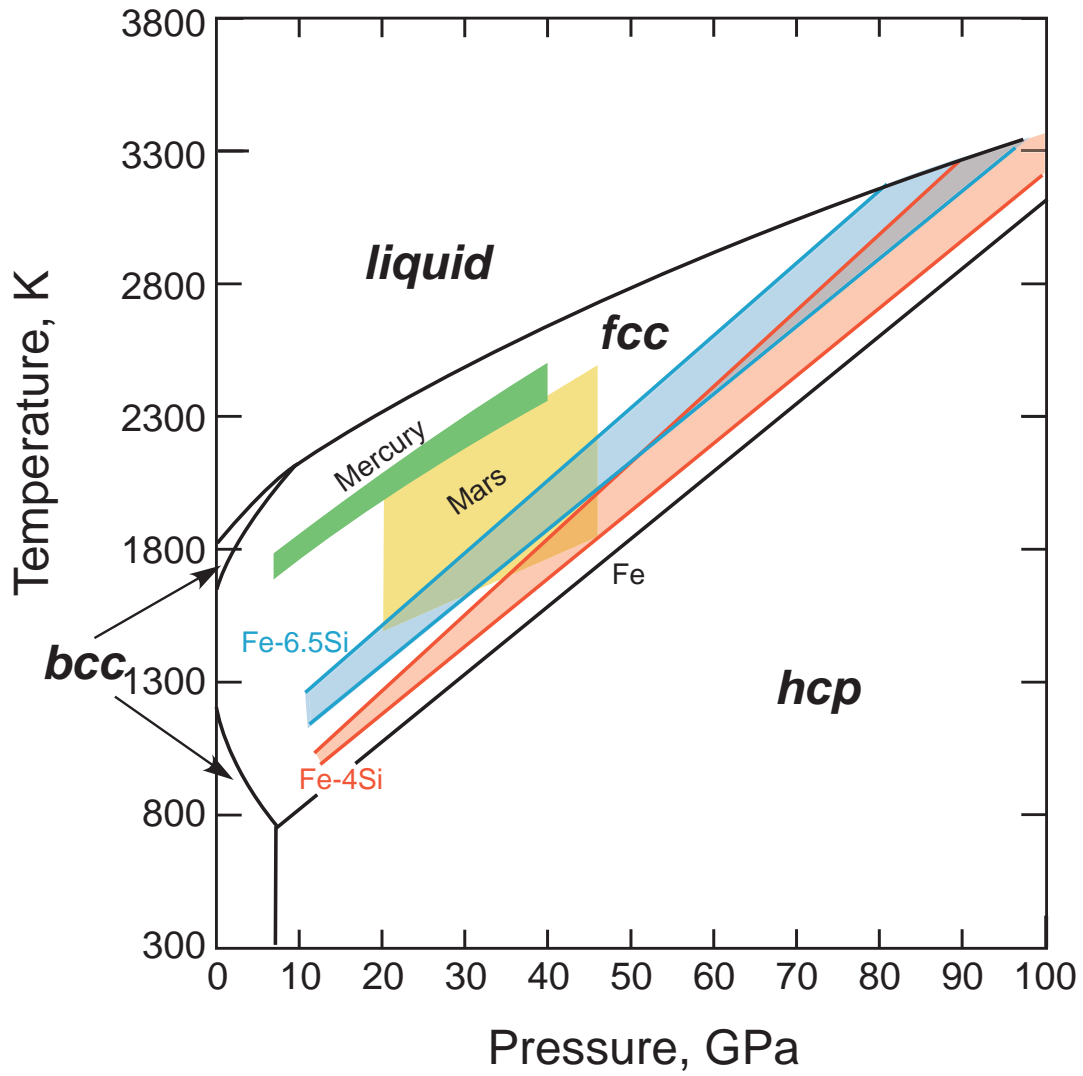


figure 4